

Pre-existing orthorhombic embryos-induced hexagonal-orthorhombic martensitic transformation in $MnNiSi_{1-x}(CoNiGe)_x$ alloy

Ting-Ting Zhang(张婷婷), Yuan-Yuan Gong(龚元元), Zi-Qian Lu(鲁子骞), and Feng Xu(徐锋)

Citation: Chin. Phys. B, 2024, 33 (**4**): 048103. DOI: 10.1088/1674-1056/ad188d
Journal homepage: http://cpb.iphy.ac.cn; http://iopscience.iop.org/cpb

What follows is a list of articles you may be interested in

High temperature strain glass in Ti-Au and Ti-Pt based shape memory alloys

Shuai Ren(任帅), Chang Liu(刘畅), and Wei-Hua Wang(汪卫华)
Chin. Phys. B, 2021, 30 (**1**): 018101. DOI: 10.1088/1674-1056/abc54a

Evolution of magnetic domain structure of martensite in Ni-Mn-Ga films under the interplay of the temperature and magnetic field

Xie Ren (谢忍), Wei Jun (韦俊), Liu Zhong-Wu (刘仲武), Tang Yan-Mei (唐妍梅), Tang Tao (唐涛), Tang Shao-Long (唐少龙), Du You-Wei (都有为)
Chin. Phys. B, 2014, 23 (**6**): 068103. DOI: 10.1088/1674-1056/23/6/068103

Relation between martensitic transformation temperature range and lattice distortion ratio of NiMnGaCoCu Heusler alloys

Wei Jun (韦俊), Xie Ren (谢忍), Chen Le-Yi (陈乐易), Tang Yan-Mei (唐研梅), Xu Lian-Qiang (许连强), Tang Shao-Long (唐少龙), Du You-Wei (都有为)
Chin. Phys. B, 2014, 23 (**4**): 048107. DOI: 10.1088/1674-1056/23/4/048107

Thermal stability and high-temperature shape memory characteristics of Ti-20Zr-10Ta alloy

Zheng Xiao-Hang (郑晓航), Sui Jie-He (隋解和), Zhang Xin (张欣), Yang Zhe-Yi (杨哲一), Cai Wei (蔡伟)
Chin. Phys. B, 2014, 23 (**1**): 018101. DOI: 10.1088/1674-1056/23/1/018101

Magnetostructural transition in NiCuCoMnGa alloys

Li Pan-Pan (李盼盼), Wang Jing-Min (王敬民), Jiang Cheng-Bao (蒋成保)
Chin. Phys. B, 2013, 22 (**8**): 088105. DOI: 10.1088/1674-1056/22/8/088105

Pre-existing orthorhombic embryos-induced hexagonal–orthorhombic martensitic transformation in $MnNiSi_{1-x}(CoNiGe)_x$ alloy

Ting-Ting Zhang(张婷婷), Yuan-Yuan Gong(龚元元), Zi-Qian Lu(鲁子骞), and Feng Xu(徐锋)†

MIIT Key Laboratory of Advanced Metallic and Intermetallic Materials Technology, School of Materials Science and Engineering, Nanjing University of Science and Technology, Nanjing 210094, *China*

(Received 18 September 2023; revised manuscript received 17 December 2023; accepted manuscript online 25 December 2023)

The thermal–elastic martensitic transformation from high-temperature Ni_2In-type hexagonal structure to low-temperature TiNiSi-type orthorhombic structure has been widely studied in Mn*MX* (*M* = Ni or Co, and *X* = Ge or Si) alloys. However, the answer to how the orthorhombic martensite nucleates and grows within the hexagonal parent is still unclear. In this work, the hexagonal–orthorhombic martensitic transformation in a Co and Ge co-substituted MnNiSi is investigated. One can find some orthorhombic laths embedded in the hexagonal parent at a temperature above the martensitic transformation start temperature (M_s). With the the sample cooing to M_s, the laths turn broader, indicating that the martensitic transformation starts from these pre-existing orthorhombic laths. Microstructure observation suggests that these pre-existing orthorhombic laths do not originate from the hexagonal–orthorhombic martensitic transformation because of the difference between atomic occupations of doping elements in the hexagonal parent and those in the pre-existing orthorhombic laths. The phenomenological crystallographic theory and experimental investigations prove that the pre-existing orthorhombic lath and generated orthorhombic martensite have the same crystallography relationship to the hexagonal parent. Therefore, the orthorhombic martensite can take these pre-existing laths as embryos and grow up. This work implies that the martensitic transformation in $MnNiSi_{1-x}(CoNiGe)_x$ alloy is initiated by orthorhombic embryos.

Keywords: martensitic transformation, Mn*MX* alloy, orthorhombic embryo, crystallography relationship

PACS: 81.30.Kf, 81.05.Bx, 68.55.A–, 61.50.Ks **DOI:** 10.1088/1674-1056/ad188d

1. Introduction

The thermal–elastic martensitic transformation is a well-known phenomenon in the field of material science, specifically, there is a crystal structure change from a high-symmetry parent to a low-symmetry martensite during cooling, in which no atomic diffusion occurs. This transformation is associated with many beneficial physical effects such as shape memory effect,[1–3] superelasticity,[1,3] elastocaloric effect,[4–6] and magnetocaloric effect.[7,8] Consequently, materials that exhibit these thermal–elastic martensitic transformations have become one of widely studied topics focusing on functional materials. It has been found that this transformation exists in Numerous compounds, including Ti–Ni-based alloys,[1,2] Heusler-type Ni–Mn-based alloys,[3–5] and Cu-based shape memory alloys,[9–11] some of which have successfully been utilized in sensors,[12] thermal energy harvesters,[13,14] and solid state refrigeration.[7]

MnCoGe, MnNiGe, MnCoSi, and MnNiSi (known as Mn*MX* (*M* = Ni or Co and *X* = Ge or Si)) are four typical intermetallics, each of which displays a unique thermal–elastic martensitic transformation from high-temperature Ni_2In-type hexagonal (space group $P63/mmc$, 194) structure to low-temperature TiNiSi-type orthorhombic (space group *Pnma*, 62) structure.[12–22] Taking MnNiSi for example, the hexagonal structure can be regarded as being comprised of flat layered Ni–Si honeycombs, which are stitched together by Mn atoms along the $[0001]_h$ axis (Figs. 1(a) and 1(b)). After the transformation from the hexagonal structure to the orthorhombic structure, all atoms move relative to their initial positions, and in the orthorhombic structure the atomic chains are arranged in zigzag pattern (Figs. 1(c) and 1(d)). In the two structures, Si and Ni atoms with close atomic spacing are linked by covalent bonds, while Mn atoms are relatively isolated. MnCoGe and MnNiGe undergo the hexagonal–orthorhombic martensitic transformation at about 450 K,[15–25] while MnCoSi and MnNiSi have higher transformation temperatures (T_t) above 1100 K.[26–31] In previous investigations on Mn*MX* alloys, foreign atoms such as B,[19] Fe,[23,24] Cu,[32] Ga,[33] and Sn,[34] were introduced to suitably tune the T_t, so that $T_{C,h} < T_t < T_{C,o}$ ($T_{C,h}$ and $T_{C,o}$ indicate the Curie temperatures of the hexagonal phase and orthorhombic phase, respectively). In this case, the hexagonal–orthorhombic martensitic transformation occurs between the paramagnetic hexagonal phase and the ferromagnetic orthorhombic phase. This transformation can be induced by a magnetic field, producing fascinating magneto-functional properties.[27,35,36] Although numerous studies have suggested effective methods to tune the T_t and bring about transformation-associated physical effects, the question of how the orthorhombic martensite nucleates and grows within the hexagonal parent phase remains open.

†Corresponding author. E-mail: xufeng@njust.edu.cn

© 2024 Chinese Physical Society and IOP Publishing Ltd

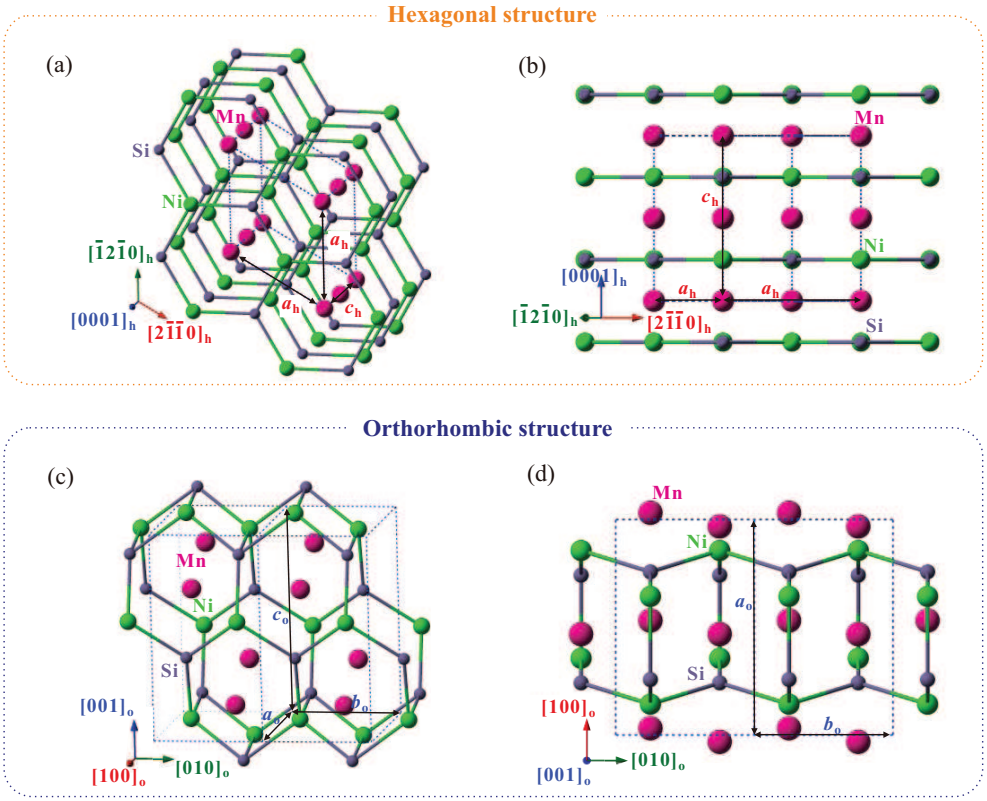


Fig. 1. (a) Crystal structure of hexagonal MnNiSi. (b) Atomic arrangement of hexagonal MnNiSi with $[01\text{-}10]_h$ vertical to the paper. (c) Crystal structure of orthorhombic MnNiSi. (d) Atomic arrangement of orthorhombic MnNiSi with $[001]_o$ vertical to the paper. Subscripts h and o correspond to the hexagonal structure and orthorhombic structure, respectively.

The nucleation and growth of martensite have been a focal point for martensitic transformation researchers for decades. Early studies attempted to explain the nucleation of martensite by using classical homogeneous nucleation theory.[37] However, the calculated Gibbs free energy difference between martensite nuclei and the parent material cannot be overcome by thermal energy,[38] indicating that heat alone is insufficient to trigger off the martensitic transformation. Subsequently, researchers proposed that the nucleation of martensite is a heterogeneous process.[39–46] They suggested that field stress and lattice strain around pre-existing defects, such as dislocations, promote the nucleation of martensite. This theory is supported by molecular dynamics,[47] numerical simulation,[48] and *in-situ* TEM observations in Ti–Ni, Ti–Ni–Cu, and Cu–Al–Ni alloys.[49–51] Clapp took it one step further by proposing a local soft-mode theory.[52] This theory suggests that when approaching T_t, the lattice structure becomes unstable due to the softening of a specific lattice vibration mode. As a result, the stress field near defects can cause the unstable lattice to transform into martensite. In put it another way, theoretical researches and experimental studies support the notion that the defects aid in martensite nucleation.

Unlike the nucleation models related to defects, Knapp and Dehlinger assumed that martensitic embryos pre-exists in the parent material, and therefore, the nucleation and growth of martensite do not need to overcome the energy barrier mentioned in classical homogeneous nucleation theory.[53] These embryos remain dormant until they approach the martensitic transformation start temperature, triggering off the transformation. Regrettably, there has been a lack of direct experimental evidence to support the existence of these pre-existing martensitic embryos in any given material.

In this work, we present our findings from microstructural observations on MnNiSi alloy that has been co-substituted with Co and Ge. Our investigations reveal that there are thin orthorhombic laths existing in the hexagonal matrix, even though the temperature does not reach its T_t. These laths are observed to expand during cooling, providing the evidence that they serve as pre-existing embryos, which play an important role in facilitating the hexagonal–orthorhombic martensitic transformation.

2. Experiment

Polycrystalline ingot with a nominal composition of $Mn_{0.625}Co_{0.375}NiSi_{0.625}Ge_{0.375}$ was prepared by arc-melting high-purity raw materials under an argon atmosphere three times. The as-cast ingot was annealed in evacuated quartz tubes at 1073 K for five days, followed by quenching into water. The crystal structure of the sample was identified by using powder x-ray diffraction (XRD, Bruker D8 Advance) with Cu-$K\alpha$ radiation at room temperature. For the temperature-dependent XRD measurement, patterns were collected by using a PANalytical X-pert Pro diffractometer equipped with an

Anton Paar TTK450 low-temperature chamber. The structure refinement of XRD patterns was performed by using Fullprof's implementation of the Rietveld refinement method. The magnetic measurements of initial cooling process were performed by using a cryogen-free physical property measurement system (PPMS Dynacool^{TM} Quantum Design) with a vibrating sample magnetometer. Magnetic measurement was performed on a bulk sample with mass of $\sim$ 23 mg. The microstructure was examined by using an optical microscope equipped with a temperature-controlled stage. Prior to the observation, the surface was carefully mechanically polished then corroded for 10 s at room temperature by aquaregia. Conventional transmission electron microscope (TEM) measurement was performed on an FEI Tecnai G2 F20 microscope. The high-resolution transmission electron microscope (HRTEM) and scanning transmission electron microscope (HRSTEM) observations were carried out by using an FEI Titan Themis microscope. The sample for TEM measurement was prepared by using ion beam milling technique.

3. Results and discussion

3.1. Hexagonal–orthorhombic martensitic transformation in $Mn_{0.625}Co_{0.375}NiSi_{0.625}Ge_{0.375}$

According to previous research, co-substitution of Co and Ge can effectively reduce the T_t of MnNiSi from 1200 K to room temperature.[31] This co-substitution triggers off a martensitic transformation between paramagnetic hexagonal phase and ferromagnetic orthorhombic phase, thus magnetic measurements can be used to track the transformation. The temperature-dependent magnetization curves of the $Mn_{0.625}Co_{0.375}NiSi_{0.625}Ge_{0.375}$ polycrystal under 0.1 T are shown in Fig. 2(a). The sudden increase in magnetization during cooling (and decrease during heating) signifies the occurrence of the martensitic transformation from hexagonal to orthorhombic (and *vice versa*). The presence of thermal hysteresis, indicated by the misalignment between the heating curve and cooling curve, provides the evidence for the first-order nature of this phase transformation. The M_s, M_f, A_s, and A_f temperatures, denoting the onset of martensitic transformation, the end of martensitic transformation, the onset of austenitic transformation, and the end of austenitic transformation, respectively, are 268 K, 258 K, 305 K, and 321 K, as shown in Fig. 2(a). The temperature-dependent XRD patterns in cooling process (from 150 °C to target temperatures) are illustrated in Fig. 2(b). At 300 K, which is 32 K higher than M_s, the predominant hexagonal phase is accompanied by faint traces of the orthorhombic phase. However, when cooling to 260 K, a temperature between M_s and M_f, the orthorhombic phase takes over as the dominant phase. An optical image of the $Mn_{0.625}Co_{0.375}NiSi_{0.625}Ge_{0.375}$ polycrystal cross-section at room temperature is shown in Fig. 2(c) and displays three straight and black parallel lines. As found in previous investigations,[54–57] these lines correspond to thin laths in the orthorhombic structure. The optical observation is corroborated well with the XRD patterns obtained at 300 K (Fig. 2(b)). Nonetheless, this raises the question of why the orthorhombic phase appears at a temperature higher than M_s.

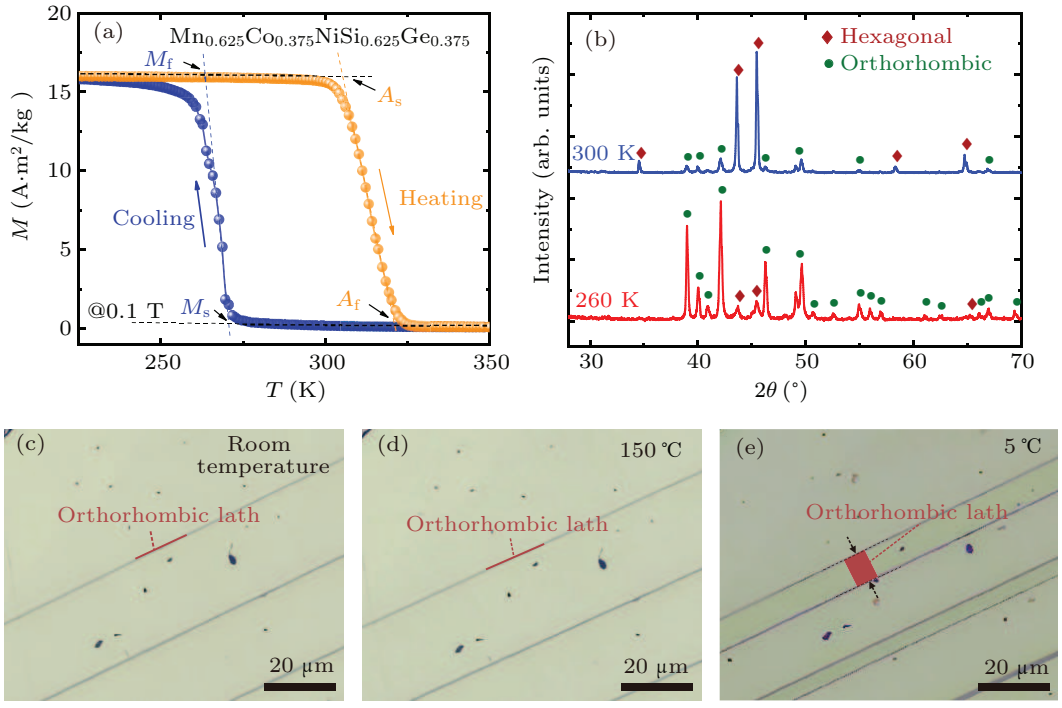


Fig. 2. (a) Temperature-dependent magnetization curves of $Mn_{0.625}Co_{0.375}NiSi_{0.625}Ge_{0.375}$ polycrystal under 0.1 T. (b) XRD patterns of $Mn_{0.625}Co_{0.375}NiSi_{0.625}Ge_{0.375}$ powder at 300 K and 260 K. Optical image of cross section of $Mn_{0.625}Co_{0.375}NiSi_{0.625}Ge_{0.375}$ polycrystal at (c) room temperature, (d) 150 °C, and (e) 5 °C.

To address this question, we conduct further investigations of the microstructure changes during temperature fluctuations, by employing an optical microscope with a temperature-controlled stage. Interestingly, when the temperature is raised to 150 °C, a temperature significantly higher than A_f, it is observed that the straight lines persist, and the morphology remains the same as that at room temperature (Fig. 2(c)). This finding suggests that these black lines may be inherently stable in the hexagonal parent, even when subjected to further heating. When cooling to 5 °C, a temperature highly proximate to M_s, the black lines become broader, indicating the onset of the hexagonal–orthorhombic martensitic transformation and the growth of the pre-existing orthorhombic laths. Further cooling causes a significant amount of orthorhombic martensite to form and the sample to fragment into powders due to the large lattice distortion during the hexagonal–orthorhombic martensitic transformation.

The formation of martensite is accompanied by high strain energy, which is reduced near surfaces, leading to a phenomenon known as "surface martensite".[58–60] However, this effect will only cause minor changes in M_s temperature, and cannot account for a difference of hundreds of degrees Celsius.[61] In fact, despite different strain fields, the M_s temperature of spontaneous transformation to martensite and the M_s temperature of stress-induced transformation in a single crystal or polycrystal do not show substantial differences.[62] Therefore, Wayman[63] proposed that we distinguish between "martensite formed at a surface" and "surface martensite". The strain direction and orientation of the former are the same as those of a bulk sample, while the latter has a morphology different from bulk alloy due to the low phase transition drive and independent crystallographic characteristics. In the case of the $Mn_{0.625}Co_{0.375}NiSi_{0.625}Ge_{0.375}$ alloy, the orthorhombic laths observed at temperatures higher than 150° above M_s cannot reasonably be attributed to "surface martensite". The orientation measurements discussed in Subsection 3.4 will further support this statement.

3.2. Atomic structures of pre-existing orthorhombic laths and hexagonal parent

The TEM image presented in Fig. 3(a) shows the case of an 80-nm-thick foil, revealing a pre-existing orthorhombic lath with a width of 390 nm embedded in the hexagonal parent structure. The selected-area electron diffraction patterns of the hexagonal matrix displayed in Fig. 3(b) are in complete agreement with those of the hexagonal MnNiSi with $[01\text{-}10]_h$ incidence (Fig. 3(c)), indicating uniformity and consistency in the structure. Despite high substitution levels of Co and Ge reaching to 37.5%, no additional super-lattice diffraction spots are detected in the sample. To better understand the influence of atomic substitution on diffraction spots, we meticulously carried out the simulations of electron diffraction patterns for all possible long-range ordered hexagonal structures that share the same composition as $Mn_{0.5}Co_{0.5}NiSi_{0.5}Ge_{0.5}$. In these hexagonal structures, we replace Mn and Si with Co and Ge in various scenarios, including: (i) orderly replacement of Mn and Si by Co and Ge, respectively (as shown in unit-cell I_h in Fig. 3(d)); (ii) disorderly replacement of Mn by Co and orderly replacement of Si by Ge (II_h in Fig. 3(d)); (iii) orderly replacement of Mn by Co and disorderly replacement of Si by Ge (III_h in Fig. 3(d)); and (iv) disorderly replacement of Mn and Si by Co and Ge, respectively (IV_h in Fig. 3(d)). For in-depth details regarding atomic occupation in the hexagonal $Mn_{0.5}Co_{0.5}NiSi_{0.5}Ge_{0.5}$, refer to Table S1, please. We observed additional diffraction spots at $\{0001\}_h$, $\{\text{-}2111\}_h$, and $\{\text{-}4221\}_h$ positions in the simulated electron diffraction patterns of I_h and II_h (marked by green circles in Fig. 3(e)). Furthermore, for III_h, additional diffraction spots emerged at $\{0001\}_h$ and $\{\text{-}4221\}_h$ positions (marked by green circles in Fig. 3(f)). Only when the atomic configuration is the same as IV_h, are the simulated diffraction patterns consistent with those shown in Fig. 3(c). The ratios of intensity for $\{0001\}_h$, $\{\text{-}2111\}_h$, and $\{\text{-}4221\}_h$ to the brightest $\{\text{-}2110\}_h$ are presented in Table 1. Notably, the intensity of $\{0001\}_h$ and $\{\text{-}4221\}_h$ for III_h are remarkably weak and invisible in experimental data. Consequently, the simulated electron diffraction patterns of III_h and IV_h can be consistent with experimental results. Both structures demonstrate a disordered occupation of Ge atoms in the hexagonal parent.

Table 1. Intensity ratios of $\{0001\}_h$, $\{\text{-}2111\}_h$, and $\{\text{-}4221\}_h$ to $\{\text{-}2110\}_h$ in simulated electron diffraction patterns of I_h, II_h, III_h, and IV_h.

	$I_{\{0001\}}/I_{\{\text{-}2110\}}$ (%)	$I_{\{\text{-}2111\}}/I_{\{\text{-}2110\}}$ (%)	$I_{\{\text{-}4221\}}/I_{\{\text{-}2110\}}$ (%)
I_h	0.697	0.451	0.203
II_h	0.662	0.450	0.201
III_h	0.040	0.000	0.001
IV_h	0.000	0.000	0.000

The electron diffraction patterns of the pre-existing orthorhombic lath are displayed in Fig. 4(a). It can be observed that additional diffraction spots at $\{010\}_o$ positions are present (highlighted by the red circle in Fig. 4(a)) in comparison with those of the orthorhombic MnNiSi with $[001]_o$ incidence (Fig. 4(b)). In order to confirm the relationship between these additional diffraction spots and atomic substitution, several assumed orthorhombic structures are simulated. Initially, simulations are performed on $Mn_{0.75}Co_{0.25}NiSi_{0.75}Ge_{0.25}$ where one Mn atom is replaced by a Co atom, while one Si atom is substituted by a Ge atom in the unit-cell of the orthorhombic MnNiSi. The fractional coordinates of each atom in the orthorhombic MnNiSi can be found in Table S2. The simulated electron diffraction patterns for all possible structures

along the $[001]_o$ incidence direction are depicted in Fig. S1. The $\{010\}_o$ diffraction spots are present as long as Ge atoms orderly replace Si atoms or Co atoms orderly replace Mn atoms. However, With the $\{010\}_o$ diffraction spots appearing, additional $\{100\}_o$ diffraction spots with a similar diffraction intensity are also present. The intensity ratios of $\{010\}_o$ and $\{100\}_o$ to the brightest $\{020\}_o$ in the simulated electron diffraction patterns can be found in Table S3. As shown in Fig. 4(a), there are found no discernible $\{100\}_o$ diffraction spots. This suggests that the observed $\{010\}_o$ diffraction spots are unlikely to be attributed to the presence of orthorhombic $Mn_{0.75}Co_{0.25}NiSi_{0.75}Ge_{0.25}$.

Afterwards, we proceed to simulate the electron diffraction patterns of orthorhombic $Mn_{0.5}Co_{0.5}NiSi_{0.5}Ge_{0.5}$, where Co atoms replace two Mn atoms and Ge atoms replace two Si atoms. Fifteen possible orthorhombic structures are considered (their details are indicated in Table S4), of which four exhibit similar electron diffraction patterns as seen in Fig. 4(a). As displayed in Fig. 4(c), the unit-cells of the four orthorhombic structures are marked as I_o, II_o, III_o, and IV_o, respectively, with their atomic occupations listed in Table 2. Notably, four structures all share a common characteristic, i.e., Si_1 & Si_4 atoms are replaced by Ge atoms. The electron diffraction patterns of I_o and II_o are simulated and the results are shown in Fig. 4(d). Notably, in addition to $\{010\}_o$ spots, $\{100\}_o$ diffraction spots can be observed. However, the intensity ratio of $\{100\}_o$ is extremely weak, making the experimental spots possibly invisible. To provide a quantitative comparison, Table 2 summarizes the intensity ratios of $\{100\}_o$ and $\{010\}_o$ with respect to the brightest $\{020\}_o$ in the simulated electron diffraction patterns of I_o, II_o, III_o, and IV_o. Moreover, the electron diffraction patterns of III_o and IV_o depicted in Fig. 4(e) are shown to be consistent with the experimental results presented in Fig. 4(a). This highlights that the $\{010\}_o$ diffraction spots originate from orthorhombic $Mn_{0.5}Co_{0.5}NiSi_{0.5}Ge_{0.5}$, where Ge atoms take the positions of Si atoms in an orderly manner.

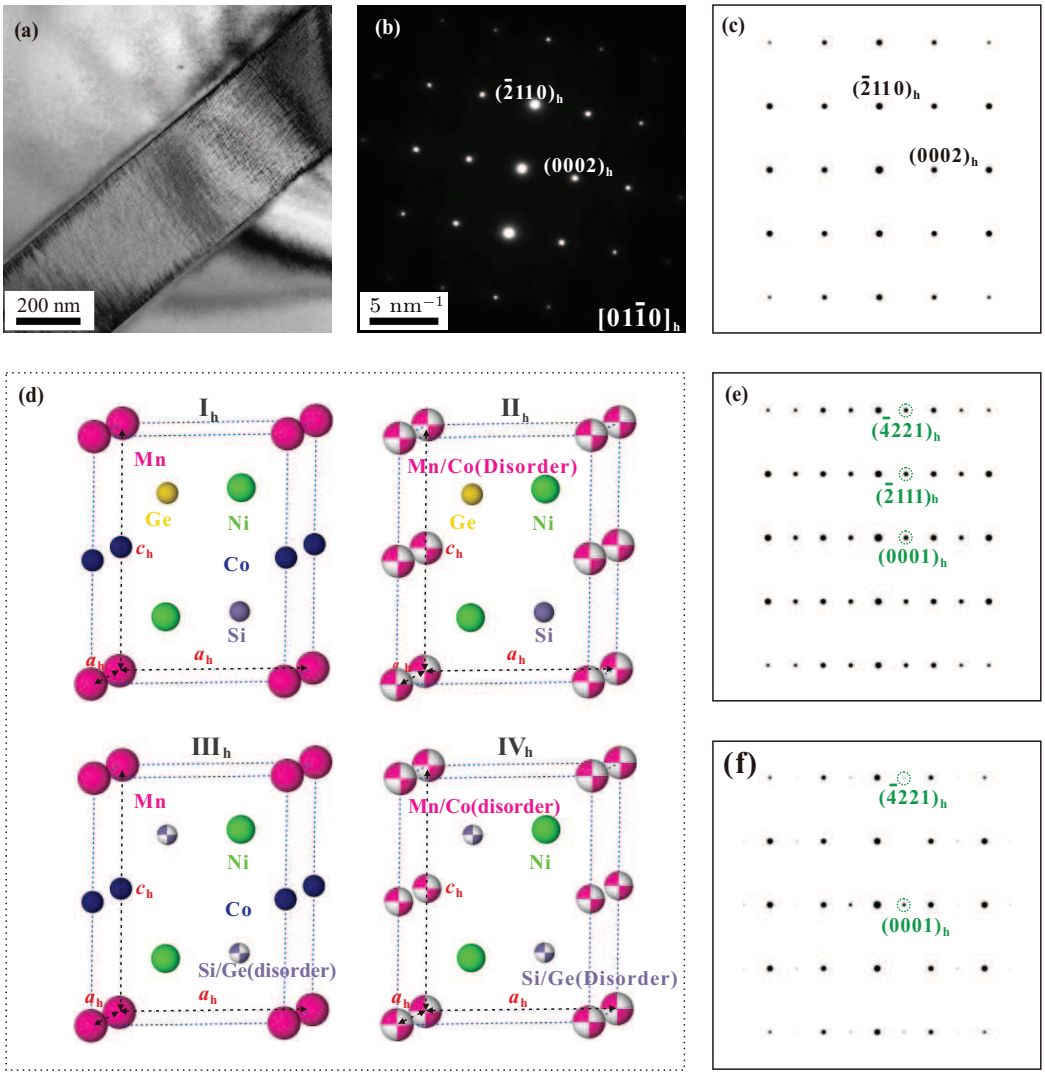


Fig. 3. (a) TEM image of foil, in which one pre-existing orthorhombic lath is embedded in hexagonal parent. (b) Selected-area electron diffraction patterns of hexagonal parent. (c) Selected-area electron diffraction patterns of hexagonal MnNiSi with $[01\text{-}10]_h$ incidence. (d) Four assumed hexagonal structures (marked by I_h, II_h, III_h, and IV_h) with the same composition of $Mn_{0.5}Co_{0.5}NiSi_{0.5}Ge_{0.5}$. (e) Simulated electron diffraction patterns of I_h and II_h with $[01\text{-}10]_h$ incidence. (f) Simulated electron diffraction patterns of III_h with $[01\text{-}10]_h$ incidence.

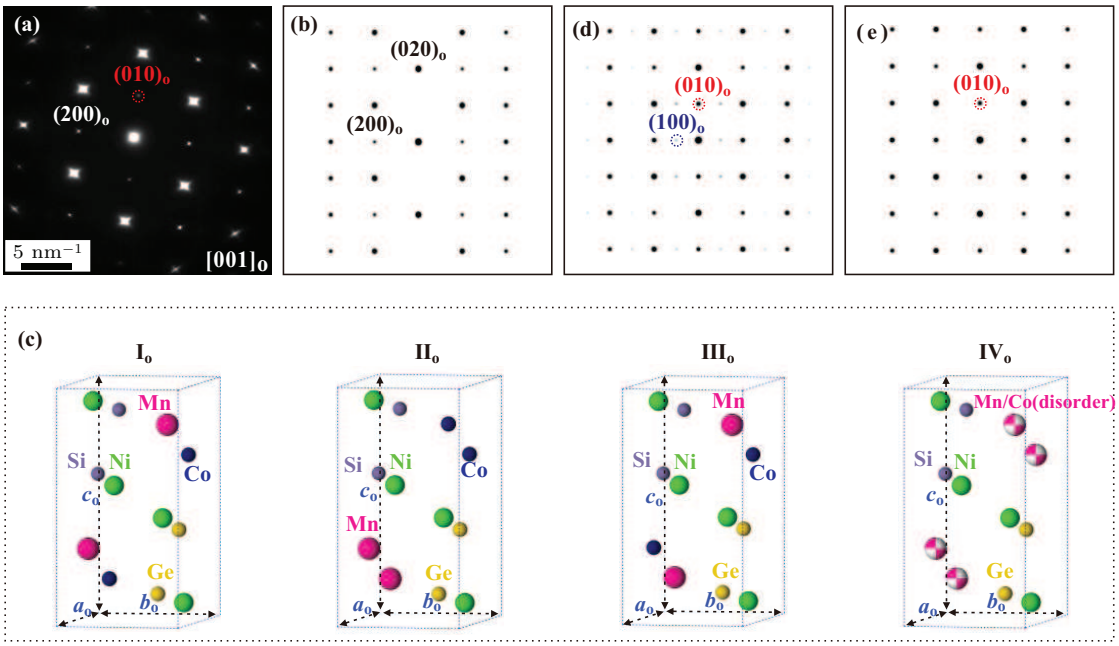


Fig. 4. (a) Selected-area electron diffraction patterns of orthorhombic lath. (b) Simulated electron diffraction patterns of orthorhombic MnNiSi with $[001]_o$ incidence. (c) Four assumed orthorhombic structures (marked by I_o, II_o, III_o, and IV_o) with the same composition of $Mn_{0.5}Co_{0.5}NiSi_{0.5}Ge_{0.5}$. (d) Simulated electron diffraction patterns of I_o and II_o with $[001]_o$ incidence. (e) Simulated electron diffraction patterns of III_o and IV_o with $[001]_o$ incidence.

Table 2. Atomic occupation and intensity ratios of $\{100\}_o$ and $\{010\}_o$ to $\{020\}_o$ in the simulated electron diffraction patterns of I_o, II_o, III_o, and IV_o.

	Atomic occupation	$I_{\{100\}}/I_{\{020\}}$ (%)	$I_{\{010\}}/I_{\{020\}}$ (%)
I_o	Co replaces Mn_1 & Mn_2 and Ge replaces Si_1 & Si_4	0.003	0.833
II_o	Co replaces Mn_1 & Mn_4 and Ge replaces Si_1 & Si_4	0.067	0.833
III_o	Co replaces Mn_1 & Mn_3 and Ge replaces Si_1 & Si_4	0.0	0.637
IV_o	Co disorderly replaces Mn while Ge replaces Si_1 & Si_4	0.0	0.833

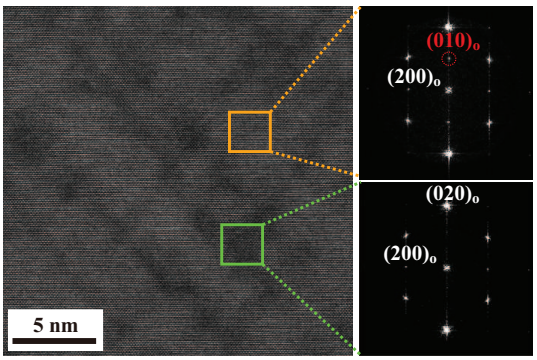


Fig. 5. HRSTEM images of orthorhombic lath under $[001]_o$ incidence and fast Fourier transform results from regions in orange and green boxes.

Figure 5 shows the HRSTEM images of the pre-existing orthorhombic lath, captured with $[001]_o$ incidence. The fast Fourier transform outcomes from various regions are also displayed. The $\{010\}_o$ diffraction spots can be identified effortlessly when the fast Fourier transform is taken from the region highlighted with an orange box. On the other hand, these spots are absent if the region is changed to a green box. The fast Fourier transform results derived from the green box are identical to the electron diffraction patterns of the orthorhombic MnNiSi with $[001]_o$ incidence (see Fig. 4(b)). This indicates that the occupation of Ge atoms is disordered. As a consequence, the lath consists of two orthorhombic phases. In one phase, Ge atoms orderly replace Si atoms, while in the other, the occupation of Ge atoms is disordered.

In other words, the occupation of Ge atoms presents a discrepancy between the hexagonal parent and the pre-existing orthorhombic laths. In the hexagonal parent, Ge atoms are entirely disordered, whereas in some areas of the pre-existing orthorhombic lath, they replace Si atoms in an orderly manner. This fact indicates that the pre-existing orthorhombic lath does not result from the hexagonal–orthorhombic martensitic transformation which is diffusionless, and that the martensite should inherit the atomic ordering of its parent structure. If Ge atoms are randomly distributed in the hexagonal parent, their occupation in the orthorhombic martensite should also be disordered. Therefore, we believe that the unique atomic arrangement plays a critical role in facilitating the stable coexistence of these pre-existing orthorhombic laths within the hexagonal matrix.

3.3. Crystallography of hexagonal–orthorhombic martensitic transformation

Before we delve into the relationship between the pre-existing orthorhombic lath and the hexagonal parent, it is crucial to comprehend the crystallography of the hexagonal–orthorhombic martensitic transformation. To obtain the lattice parameters of the hexagonal parent and orthorhombic martensite, our sample is cooled to a temperature between M_s and M_f, and its XRD patterns are refined (refer to Fig. 6). The obtained values are as follows: $a_h = 0.397$ nm, $c_h = 0.515$ nm (for hexagonal parent), and $a_o = 0.569$ nm, $b_o = 0.366$ nm, and $c_o = 0.694$ nm (for orthorhombic martensite).

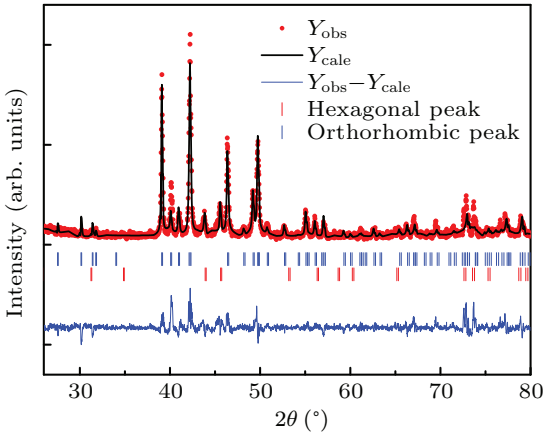


Fig. 6. Refined XRD patterns at a temperature between M_s and M_f.

According to previous researches,[23,24] the relationship between the hexagonal structure and orthorhombic structure follows $c_h \to a_o$, $a_h \to b_o$, and $\sqrt{3}a_h \to c_o$. This relationship is expressed in the rectangular coordinate system with $X = [0001]_h||[100]_o$, $Y = [2\text{-}1\text{-}10]_h||[010]_o$, and $Z = [01\text{-}10]_h||[001]_o$ for clarity (Fig. 7(a)). Accordingly, the lattice parameters of the two structures are connected through a Bain strain:

$$\begin{bmatrix} a_o \\ b_o \\ c_o \end{bmatrix} = \begin{bmatrix} a_o/c_h & & \\ & b_o/a_h & \\ & & c_o/\sqrt{3}a_h \end{bmatrix} \begin{bmatrix} c_h \\ a_h \\ \sqrt{3}a_h \end{bmatrix} = \begin{bmatrix} 1.106 & & \\ & 0.921 & \\ & & 1.008 \end{bmatrix} \begin{bmatrix} c_h \\ a_h \\ \sqrt{3}a_h \end{bmatrix}. \quad (1)$$

Based on the phenomenological crystallographic theory,[64] on the assumption that the yellow sphere shown in Fig. 7(b) represents the hexagonal parent, the Bain strain will transform it into the green ellipsoid. Since $c_o/\sqrt{3}a_h$ is almost equal to 1,[23,24,29,30,35,65,66] we assume that there is no change in length along the $[01\text{-}10]_h$ direction (It should be noted that in most of reported results of MnMX alloys, $c_o/\sqrt{3}a_h$ deviates from 1 and the deviation value is thought to be highly related with thermal hysteresis.[24] In our material, $c_o/\sqrt{3}a_h$ is 1.008, which is considerably higher than the counterparts in some low-hysteresis MnMX alloys.[67] This is likely to be the reason for the noticeable thermal hysteresis observed in our material). As a diffusionless martensitic transformation, there must be a habit plane in which vectors do not strain or rotate during the transformation. In Fig. 7(b), only the vectors in the blue plane (such as OA, where the sphere and ellipsoid meet at point A) are not strained, but rotated by an angle of θ from their initial position (OA'). Therefore, the Bain strain does not imply that the hexagonal structure transforms into the orthorhombic structure through expansion along $[0001]_h$ and shrinkage along $[2\text{-}1\text{-}10]_h$ because the need for a habit plane is eliminated. To create a habit plane, it is necessary to contrarotate the ellipsoid along the Z axis by θ so that all the vectors in the blue plane return to their initial positions. In this case, the red plane shown in Fig. 7(b) is simply the habit plane in the hexagonal parent. This rotation operation can be expressed as a simple equation

$$R = \begin{bmatrix} 0.9959 & -0.0905 & 0 \\ 0.0905 & 0.9959 & 0 \\ 0 & 0 & 1 \end{bmatrix}. \quad (2)$$

In the phenomenological crystallographic theory[64] of martensitic transformation, a martensitic transformation can be accomplished through a strain expressed as

$$P_1 = RBP_2. \quad (3)$$

Equations (1) and (2) express R and B for the hexagonal–orthorhombic martensitic transformation. P_2 is a simple shear that ensures the sphere is tangent to the ellipsoid. However, since $c_o/\sqrt{3}a_h$ is assumed to be 1, the sphere has been tangent to the ellipsoid. Therefore, P_2 becomes an identity matrix during this transformation. Based on the lattice parameters of the hexagonal structure and orthorhombic structure, the habit plane and strain P_1 can be determined in theory. The analysis shows that the habit plane is $\{\text{-}2113.14\}$ and P_1 in rectangular coordinates as shown in Fig. 7(b) is expressed as

$$P_1 = \begin{bmatrix} 1.1013 & -0.0834 & 0 \\ 0.1001 & 0.9176 & 0 \\ 0 & 0 & 1 \end{bmatrix}. \quad (4)$$

According to the preceding description of the crystallography of the hexagonal–orthorhombic martensitic transformation, it is possible to establish all feasible orientation relationships between the hexagonal parent and the orthorhombic martensite. For instance, if we consider $[2\text{-}1\text{-}13]_h$, it is nearly parallel to the $[110]_o$ orientation. Theoretical calculations show that there is only a 0.21° angle difference between the two orientations. Additionally, combined with $[01\text{-}10]_h||[001]_o$, one orientation relationship can be established as $[01\text{-}10]_h||[001]_o$ & $(\text{-}2112)_h||(2\text{-}20)_o$.

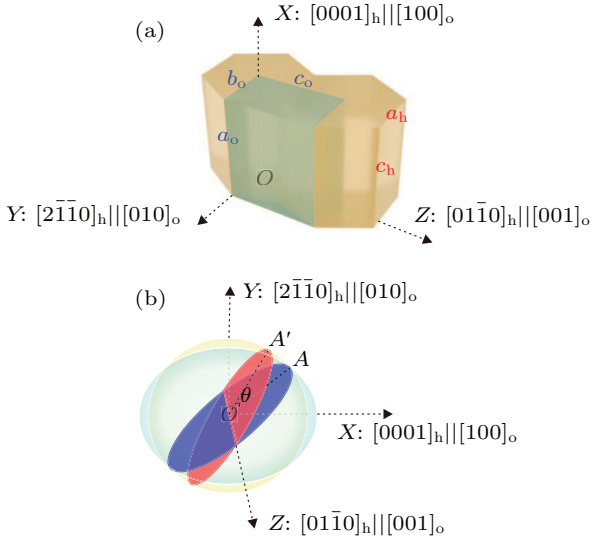


Fig. 7. (a) Schematic diagram of relationship between the hexagonal structure and orthorhombic structure. (b) Sphere-ellipsoid transformation model, with yellow sphere and green ellipsoid denoting hexagonal structure and orthorhombic structure, respectively.

3.4. Crystallographic relationship between pre-existing orthorhombic lath and hexagonal parent

In this subsection, we will uncover the crystallographic relationship between the pre-existing orthorhombic lath and the hexagonal parent. Figure 8(a) shows an HRSTEM image of an area where the hexagonal parent and the pre-existing orthorhombic lath coexist, under $[01\text{-}10]_h$ incidence. The hexagonal parent and pre-existing orthorhombic lath are located in the top-right and bottom-left corners, respectively. The EDS mapping in Fig. S2 proves that there is no difference in composition between the laths and hexagonal parent. Figure 8(b) displays a magnified HRSTEM image of the hexagonal parent. The atomic arrangement is consistent with the counterpart in Fig. 1(b), with $[01\text{-}10]_h$ oriented vertically and $[2\text{-}1\text{-}10]_h$ horizontally. The measured interspace of $(\text{-}2110)_h$ is 0.203 nm. Figure 8(c) shows a magnified HRSTEM of the pre-existing orthorhombic lath. The arrangement of atoms conforms to the arrangement in Fig. 1(d), with $[001]_o$ in vertical direction and $[010]_o$ in the horizontal direction. The interspace obtained for $(010)_o$ is 0.367 nm. The selected-area electron diffraction pattern of the region where the hexagonal parent and pre-existing orthorhombic lath coexist is illustrated in Fig. 8(d). The pattern confirms the orientation relationship between the hexagonal parent and the pre-existing orthorhombic lath, which is $[01\text{-}10]_h||[001]_o$ and $(\text{-}2112)_h||(2\text{-}20)_o$, consistent with the phenomenological crystallographic theory discussed earlier. The habit plane (-2113.14) is also marked in Fig. 8(a) located at the interface of the hexagonal parent and the pre-existing orthorhombic lath. These findings suggest that despite different atomic configurations existing, the crystal relationship of the pre-existing orthorhombic laths with the hexagonal parent and the crystal relationship of orthorhombic martensite with the hexagonal parent are similar. Moreover, the orthorhombic martensite can use these pre-existing laths as the initial point and continue to grow. This explains why the pre-existing orthorhombic laths become wider during cooling, as shown in Fig. 2.

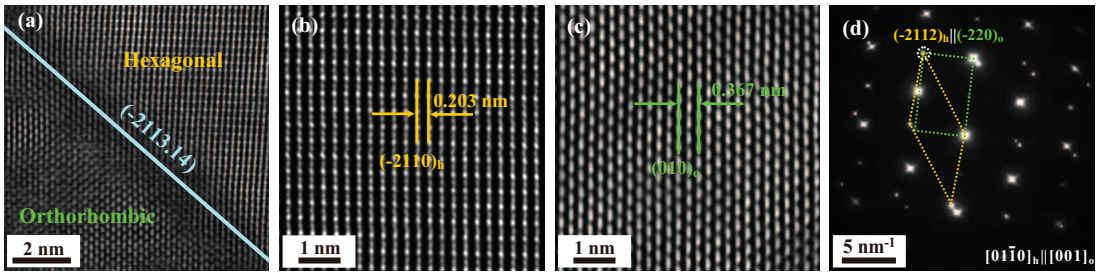


Fig. 8. (a) HRSTEM image of an area where hexagonal parent and pre-existing orthorhombic lath coexist. Magnified image of (b) hexagonal parent and (c) pre-existing orthorhombic lath. (d) Selected-area electron diffraction pattern of subfigure (a).

4. Conclusions

In our study, microstructure investigations were performed on the $Mn_{0.625}Co_{0.375}NiSi_{0.625}Ge_{0.375}$ alloy which undergoes a hexagonal–orthorhombic martensitic transformation during cooling. We discover the existence of pre-existing orthorhombic laths at temperatures higher than M_s, which significantly widen as the temperature approaches M_s. Our TEM measurement indicates a divergence in the occupation of doping atoms between the pre-existing orthorhombic laths and the hexagonal parent, providing evidence that the pre-existing orthorhombic laths are not formed as a result of the hexagonal–orthorhombic martensitic transformation. Through a combination of the phenomenological crystallographic theory and HRSTEM investigation, we further establish that the pre-existing orthorhombic laths and orthorhombic martensite exhibit the same orientation relationship as the hexagonal parent. The result of this interaction is that the orthorhombic martensite uses the pre-existing laths as a foundation and grows upwards. This finding leads us to conclude that the thin laths are, in fact, pre-existing orthorhombic embryos that facilitate the hexagonal–orthorhombic martensitic transformation.

Acknowledgement

Project supported by the National Natural Science Foundation of China (Grant No. 11974184).

References

[1] Kireeva I V, Chumlyakov Y I, Vyrodova A V, Pobedennaya Z V and Marchenko E S 2022 *Mater. Lett.* **324** 132817
[2] Lu H Z, Liu L H, Yang C, Luo X, Song C H, Wang Z, Wang J, Su Y D, Ding Y F, Zhang L C and Li Y Y 2022 *J. Mater. Sci. Technol.* **101** 205
[3] Turabi A S, Karaca H E, Tobe H, Basaran B, Aydogdu Y and Chumlyakov Y I 2016 *Scripta Mater.* **111** 110
[4] Cong D Y, Xiong W X, Planes A, Ren Y, Mañosa L, Cao P Y, Nie Z H, Sun X M, Yang Z, Hong X F and Wang Y D 2019 *Phys. Rev. Lett.* **122** 255703
[5] Niu Y R, Chen H Y, Zhang X Y, Li S W, Cong D Y, Ma T Y, Li S L, Lin J P and Wang Y D 2021 *Scripta Mater.* **204** 114123
[6] Xue D Q, Yuan R H, Yang Y C, Pang J B, Zhou Y M, Ding X D, Lookman T, Ren X B, Sun J and Xue D Z 2022 *J. Mater. Sci. Technol.* **103** 8
[7] Krenke T, Duman E, Acet M, Wassermann E F, Moya X, Mañosa L and Planes A 2005 *Nat. Mater.* **4** 450
[8] Liu J, Gottschall T, Skokov K P, Moore J D and Gutfleisch O 2012 *Nat. Mater.* **11** 620
[9] Yang Q, Wang S L, Chen J, Zhou T N, Peng H B and Wen Y H 2016 *Acta Mater.* **111** 348
[10] Zárubová N, Gemperlová J, Gemperle A, Dlabáček Z, Šittner P and Novák V 2010 *Acta Mater.* **58** 5109
[11] Liu C, Zhao Y P and Yu T 2005 *Mater. Design* **26** 465
[12] Sarawate N and Dapino M 2006 *Appl. Phys. Lett.* **88** 121923
[13] Karaman I, Basaran B, Karaca H E, Karsilayan A I and Chumlyakov Y I 2007 *Appl. Phys. Lett.* **90** 172505
[14] Li C, Gong Y Y, Wang Y, Xu G Z, Chu R X, Wang Y J and Xu F 2020 *ACS Appl. Electron. Mater.* **2** 1048
[15] Zhou H, Wang D K, Li Z, Cong J Z, Yu Z, Zhao S, Jiang P, Cong D Y, Zheng X Q, Qiao K M and Zhang H 2022 *J. Mater. Sci. Technol.* **114** 73
[16] Shen F R, Zhou H B, Hu F X, Wang J T, Wu H, Huang Q Z, Hao J Z, Yu Z B, Gao Y H, Lin Y X, Wang Y, Zhang C, Yin Z, Wang J, Deng S, Chen J, He L H, Liang T J, Sun J R, Zhao T Y and Shen B G 2021 *J. Am. Chem. Soc.* **143** 6798
[17] Wei Z Y, Liu E K, Li Y, Xu G Z, Zhang X M, Liu G D, Xi X K, Zhang H W, Wang W H, Wu G H and Zhang X X 2015 *Adv. Electron. Mater.* **1** 1500076
[18] Anzai S and Ozawa K 1978 *Phys. Rev. B* **18** 2173
[19] Aznar A, Lloveras P, Kim J, Stern-Taulats E, Barrio M, Tamarit J L, Sánchez-Valdés C F, Sánchez Llamazares J L, Mathur N D and Moya X 2019 *Adv. Mater.* **31** 1903577
[20] Biswas A, Pathak A K, Zarkevich N A, Liu X, Mudryk Y, Balema V, Johnson D D and Pecharsky V K 2019 *Acta Mater.* **180** 341
[21] Dutta P, Pramanick S, Singh V, Major D T, Das D and Chatterjee S 2016 *Phys. Rev. B* **93** 134408
[22] Li Y, Zeng Q Q, Wei Z Y, Liu E K, Han X L, Du Z W, Li L W, Xi X K, Wang W H, Wang S G and Wu G H 2019 *Acta Mater.* **174** 289
[23] Liu E K, Wang W H, Feng L, Zhu W, Li G J, Chen J L, Zhang H W, Wu G H, Jiang C B, Xu H B and de Boer F 2012 *Nat. Commun.* **3** 873
[24] Liu J, Gong Y Y, You Y R, You X M, Huang B W, Miao X F, Xu G Z, Xu F and Brück E 2019 *Acta Mater.* **174** 450
[25] Zhao Y Y, Hu F X, Bao L F, Wang J, Wu H, Huang Q Z, Wu R R, Liu Y, Shen F R, Kuang H, Zhang M, Zuo W L, Zheng X Q, Sun J R and Shen B G 2015 *J. Am. Chem. Soc.* **137** 1746
[26] Gong Y Y, Wang D H, Cao Q Q, Du Y W, Zhi T, Zhao B C, Dai J M, Sun Y P, Zhou H B, Lu Q Y and Liu J 2015 *Acta Mater.* **98** 113
[27] Liu J, Gong Y Y, Zhang F Q, You Y R, Xu G Z, Miao X F and Xu F 2021 *J. Mater. Sci. Technol.* **76** 104
[28] Staunton J B, dos Santos Dias M, Peace J, Gercsi Z and Sandeman K G 2013 *Phys. Rev. B* **87** 060404
[29] Zhang C L, Wang D H, Han Z D, Qian B, Shi H F, Zhu C, Chen J and Wang T Z 2013 *Appl. Phys. Lett.* **103** 132411
[30] Chen J H, Poudel Chhetri T, Us Saleheen A, Young D P, Dubenko I, Ali N and Stadler S 2019 *Intermetallics* **112** 106547
[31] Kasimov D, Liu J, Gong Y Y, Xu G G, Xu F and Lu G W 2018 *J. Alloys Compd.* **733** 15
[32] Xiao Y N, Zhang H, Zhang Y L, Long K, W Xing C F, Liu Y W and Long Y 2018 *J. Alloys Compd.* **769** 916
[33] Dutta P, Das D, Chatterjee S, Pramanick S and Majumdar S 2016 *J. Phys. D: Appl. Phys.* **49** 125001
[34] Liu E K, Du Y, Chen J L, Wang W H, Zhang H W and Wu G H 2011 *IEEE Trans. Magn.* **47** 4041
[35] Koyama K, Sakai M, Kanomata T and Watanabe K 2004 *Jpn. J. Appl. Phys.* **43** 8036
[36] Zhang H, Li Y W, Liu E K, Tao K, Wu M L, Wang Y X, Zhou H B, Xue Y J, Cheng C, Yan T, Long K W and Long Y 2017 *Mater. Design* **114** 531
[37] Bowles J S and Mackenzie J K 1954 *Acta Metallurgica* **2** 129
[38] Olson G B and Cohen M 1982 *Theory of Martensitic Nucleation: A current Assessment* (New York: Metallurgical Soc. of AIME) pp. 1145–1164
[39] Cech R E and Turnbull D 1956 *JOM* **8** 124
[40] Greninger A B and Mooradian V G 1938 *Aime. Trans.* **128** 337
[41] Allibert C, Bernard C, Effenberg G, Nüssler H D and Spencer P J 1981 *Calphad.* **5** 227
[42] Magee C L 1971 *Metallurgical Transactions* **2** 2419
[43] Easterling K E and Miekk-Oja H M 1967 *Acta Metallurgica* **15** 1133
[44] Easterling K E and Swann P R 1971 *Acta Metallurgica* **19** 117
[45] Lecroisey F and Pineau A 1972 *Metall Mater. Trans. B* **3** 391
[46] Werner M and Seeger A 1989 *Strength of Metals and Alloys* (ICSMA 8), August 22–26, 1988, Tampere, Finland, pp. 173–178
[47] Li B, Zhang X M, Clapp P C and Rifkin J A 2004 *J. Appl. Phys.* **95** 1698
[48] Reid A C E and Olson G B 2001 *Mater. Sci. Eng. A* **309** 370
[49] Saburi T, Komatsu T, Nenno S and Watanabe Y 1986 *J. Less-Common Met.* **118** 217
[50] Fukuda T, Saburi T, Doi K and Nenno S 1992 *Mater. Tran. Jim.* **33** 271
[51] Ibarra A, Caillard D, San Juan J and Nó M L 2007 *Appl. Phys. Lett.* **90** 101907
[52] Clapp C 1973 *Phys. Stat. Sol. (b)* **57** 561
[53] Knapp H and Dehlinger U 1956 *Acta Metallurgica* **4** 289
[54] Chulist R, Straka L, Sozinov A, Tokarski T and Skrotzki W 2017 *Acta Mater.* **128** 113
[55] Zhang T T, Gong Y Y, Wang B, Cen D Y and Xu F 2022 *J. Mater. Sci. Technol.* **104** 59
[56] Ma S C, Ge Q, Yang S, Yu K, Han X Q, Liu K, Song Y, Zhang L L, Jiang Q Z, Zhong M L, Liu R H, Wang L, Li J J and Zhong Z C 2017 *J. Alloys Compd.* **729** 1190
[57] Meng X L, Sato M and Ishida A 2009 *Acta Mater.* **57** 1525
[58] Baur A P, Cayron C and Logé R E 2019 *Acta Mater.* **179** 247
[59] He B B, Huang M X, Ngan A H W and Van Der Zwaag S 2014 *Metall. Mater. Trans. A* **45** 4875
[60] Wakasa K and Wayman C 1979 *Scr. Metall.* **13** 1163
[61] Lovey C F, Ferron J, De Bernardez S L and Ahlers M 1983 *Scr. Metall.* **17** 501
[62] Ahlers M, Pascual R, Rapacioli R and Arneodo W 1977 *Mater. Sci. Eng.* **27** 49
[63] Wayman C M 1975 *Metallography.* **8** 105
[64] Wayman C M 1964 *Introduction to the crystallography of martensitic transformations* (New York: Macmillan)
[65] Bag P and Nath R 2017 *Solid State Commun.* **270** 54
[66] Chen J H, Us Saleheen A, Karna S K, Young D P, Dubenko I, Ali N and Stadler S 2018 *J. Appl. Phys.* **124** 203903
[67] Liu E K, Wei Z Y, Li Y, Liu G D, Luo H Z, Wang W H, Zhang H W and Wu G H 2014 *Appl. Phys. Lett.* **105** 062401